Supporting Information

Synergistic zinc-ion storage enabled by Cu ion in anthraquinone -preinserted vanadate: structural integrity and H^+-promoted reversible phase conversion

Kai Li, Yang Liu, Rui Tang and Yun Gong*

Department of Applied Chemistry, College of Chemistry and Chemical Engineering, Chongqing University, Chongqing 401331, P. R. China. E-mail: gongyun7211@cqu.edu.cn; Tel: +86 023 65678932

Experimental section

Materials

Vanadium pentoxide (V_2O_5) and hydrogen peroxide (H_2O_2, 30 %) were purchased from Chengdu Cologne Chemicals Co. Ltd and Shanghai Myrell Chemical Technology Co. Ltd, respectively. In addition, 2-methylanthraquinone (2-M-AQ) was obtained from Saen Chemical Technology (Shanghai) Co. Ltd. All reagents were of analytical grade and used directly. Zn foil (thickness: 0.1 mm) was obtained from Runde Metal Materials Co. Ltd. Carbon cloth (W0S1009, thickness: 0.1 mm) was purchased from Suzhou Sinero Technology Co. Ltd. Glass fiber membrane (Grade GF/D) was obtained from Whatman Company.

Synthesis of $(C_{15}H_{10}O_2)_{0.1}V_2O_5{\cdot}0.4H_2O$ [denoted as (2-M-AQ)-VO]

(2-M-AQ)-VO was obtained by one-step solvothermal method. Firstly, 50 mg V_2O_5 was dissolved into the solution of 4.5 mL deionized water and 0.5 mL H_2O_2 (30 %) under ultrasonic treatment. Meanwhile, 45 mg 2-methylanthraquinone (2-M-AQ) was dispersed in 5 mL absolute ethyl alcohol under same condition. Then the mixture was sealed in a 15 mL autoclave and maintained at 150 ^oC for 12 h. After naturally cooling to room temperature, the precipitation was washed by distilled water and ethanol, then

collected by freeze drying.

Material characterization

The structures and phase purities of the samples were detected by powder X-ray diffractometer (XRD) (PANalytical X'pert Pro MPD) with Cu Kα radiation (λ = 1.54056 Å). Fourier transform infrared (FT-IR) spectra were recorded on IR spectrometer (IRTracer-100). Thermogravimetric (TG) curve was obtained from a METTLER TOLEDO TGA2 analyzer. CH elemental analyses were measured on an Elementar Analyzer (GmbH, Germany). X-ray photoelectron spectra (XPS) were performed on an ESCALAB 250 analyzer. Electron paramagnetic resonance (EPR) spectroscopy analyses was performed using an EPR (BRUKE EMXPLUS) with the center field of 3510 G and sweep width of 100 G. The morphologies, energy-dispersive X-ray spectroscopy (EDS) and elemental mappings of the samples were detected by scanning electron microscope (SEM, Thermo Fisher Quattro S) equipped with an EDS analyzer (AMETEK). Transmission electron microscopy (TEM), high resolution TEM (HRTEM) and selected area electron diffraction (SAED) images were obtained from transmission electron microscope (TEM, Thermo Talos F200S).

Electrochemical measurement

The (2-M-AQ)-VO sample was mixed with acetylene black, graphite powder and polyvinylidene fluoride (PVDF, served as binder) with a weight ratio of 5: 2: 1: 1 using N-methyl pyrrolidone (NMP) as solvent. The obtained slurry was evenly coated onto carbon cloth and dried at 120 ^{o}C in vacuum for 6 h.

The electrochemical measurements were performed in coin cells (CR2032) using Zn foil as the counter electrode. The mass loading of active material is in the range of 2.8 ~ 3.6 mg cm^{-2}. 3 M $Zn(CF_3SO_3)_2$ or the mixture of 2.8 M $Zn(CF_3SO_3)_2$ and 0.2 M $CuSO_4$ aqueous solution was used as the electrolyte. Cyclic voltammogram (CV) and

electrochemical impedance spectroscopy (EIS) were carried out on a CHI660E electrochemical workstation. Galvanostatic charge/discharge (GCD) and galvanostatic intermittent titration technique (GITT) measurements were implemented using LAND (CT2001A) battery-test system with the voltage range from 0.2 to 1.6 V.

Density functional theory (DFT) calculations

DFT calculations were conducted to investigate the binding energies of Zn^{2+}, Cu^{+}, and H^{+} in (2-M-AQ)-VO via the Vienna ab initio simulation package (VASP).[1] The projector augmented wave (PAW) method with Perdew–Burke–Ernzerhof (PBE) functional was implemented in electronic structure calculations.[2] The cut-off energy of 500 eV and Monkhorst–Pack *k*-point mesh of 3 × 3 × 3 grid were adopted. The convergence threshold for the force and energy were set to 0.01 eV $Å^{-1}$ and 10^{-6} eV, respectively.[3]

Table S1 The details of Rietveld refinement for (2-M-AQ)-VO.

The measurement and lattice parameters for (2-M-AQ)-VO			
Diffractometer	PANalytical Empyrean	**Radiation**	Cu Kα
2-Theta (°)	5-120	**Step size (°)**	0.01313
Chemical formula	$(C_{15}H_{10}O_2)_{0.1}V_2O_5 \cdot 0.4H_2O$	**Cell Volume (Å³)**	1122.2 (4)
Crystal system	Triclinic	**Space group**	$P\bar{1}$
***a* (Å)**	11.6939 (25)	**α (°)**	89.039 (25)
***b* (Å)**	7.1174 (23)	**β (°)**	88.443 (33)
***c* (Å)**	13.4904 (30)	**γ (°)**	89.595 (14)
R_p (%)	6.10	**R_{wp} (%)**	8.53

Selected atom parameters in (2-M-AQ)-VO

Atom from V-O-V layer	**Coordinate (error)**	**Multiplicity**	**Occupancy**
V1	0.630(1), 0.716(2), 0.127(1)	2	1
V2	0.679(1), 0.331(2), 0.160(1)	2	1
V3	0.906(1), 0.014(2), 0.140(1)	2	1
V4	0.493(2), -0.013(2), 0.170(1)	2	1
V5	0.215(1), 0.803(2), 0.143(1)	2	1
V6	0.194(1), 0.186(1), 0.141(1)	2	1
V7	0.419(1), 0.391(2), 0.157(1)	2	1
V8	0.970(1), 0.485(2), 0.148(1)	2	1
O1	0.814(2), 0.522(2), 0.124(2)	2	1
O2	0.538(8), 0.560(2), 0.142(6)	2	1
O3	0.790(2), 0.194(2), 0.080(2)	2	1
O4	0.531(9), 0.257(3), 0.146(6)	2	1
O5	0.831(2), 0.868(2), 0.087(2)	2	1
O6	0.571(2), 0.894(2), 0.097(2)	2	1
O7	0.311(2), 0.986(2), 0.124(2)	2	1
O8	0.082(2), 0.965(2), 0.104(2)	2	1
O9	0.289(2), 0.310(2), 0.078(2)	2	1
O10	0.026(2), 0.263(2), 0.120(2)	2	1
O11	0.332(2), 0.635(2), 0.089(2)	2	1

O12	0.071(1), 0.609(2), 0.099(1)	2	1
O13	0.659(7), 0.781(2), 0.311(1)	2	1
O14	0.700(1), 0.320(2), 0.283(1)	2	1
O15	0.904(1), 0.042(2), 0.286(1)	2	1
O16	0.488(2), 0.021(1), 0.312(1)	2	1
O17	0.205(1), 0.768(1), 0.290(1)	2	1
O18	0.202(1), 0.189(1), 0.285(1)	2	1
O19	0.404(1), 0.465(1), 0.286(1)	2	1
O20	0.989(1), 0.488(1), 0.309(1)	2	1

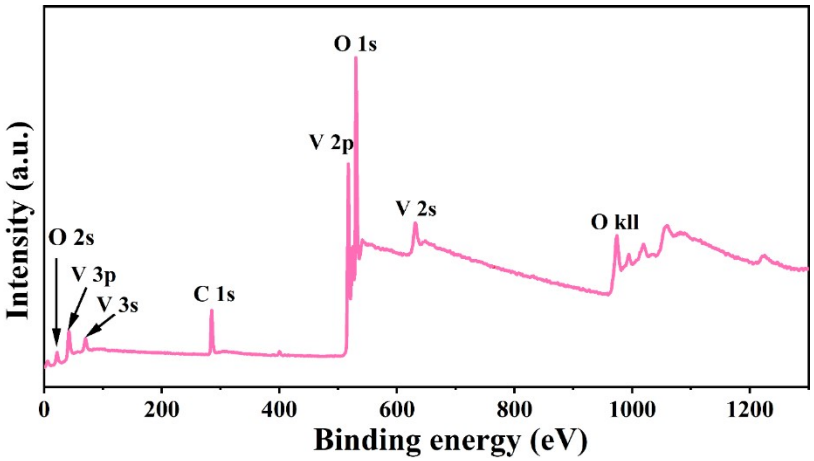

Fig. S1 The survey XPS of (2-M-AQ)-VO.

S1 The characterization of $V_2O_5 \cdot nH_2O$

The preparation of $V_2O_5 \cdot nH_2O$ was similar to that of (2-M-AQ)-VO except in the absence of 2-M-AQ. Its XRD pattern and that of the commercial V_2O_5 are shown in **Fig. S2a**. It can be seen that the commercial V_2O_5 crystallizes in orthorhombic crystal system (JCPDS No. 72-0433) with the strongest diffraction peak observed at 20.3 °. After hydrothermal reaction, the obtained $V_2O_5 \cdot nH_2O$ shows the strongest diffraction peak at 7.7 °, suggesting the interlayer spacing is expanded to be ~11.5 Å due to the intercalation of H_2O.

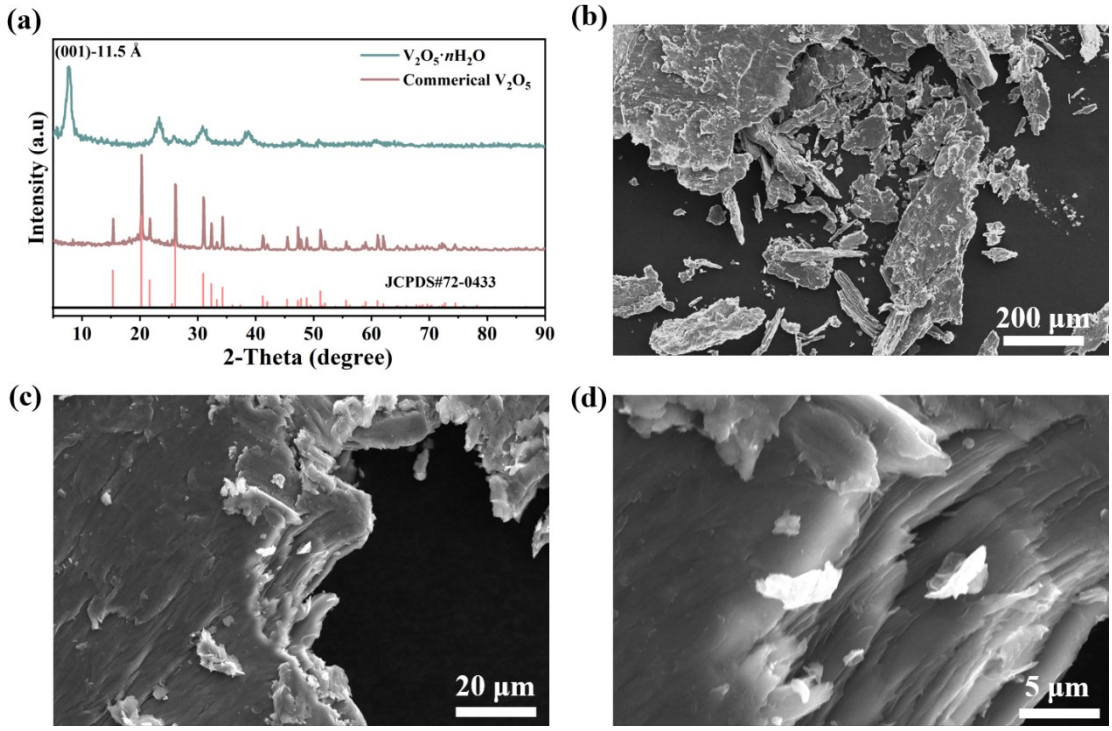

Fig. S2 (**a**) XRD patterns of $V_2O_5 \cdot nH_2O$, the commercial V_2O_5 and the standard profile; (**b-d**) SEM images of $V_2O_5 \cdot nH_2O$.

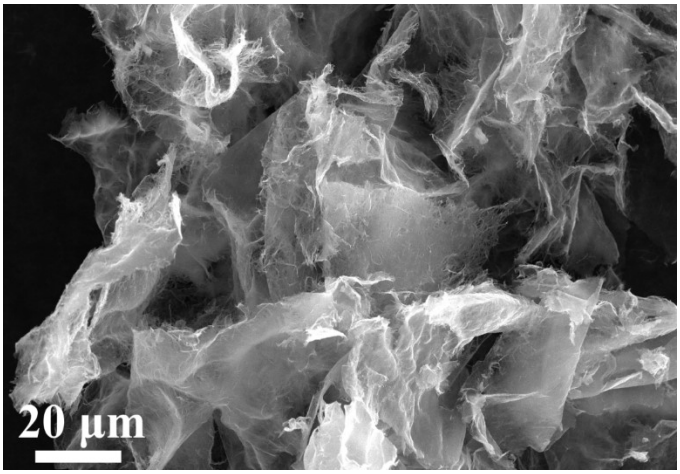

Fig. S3 The SEM image of (2-M-AQ)-VO.

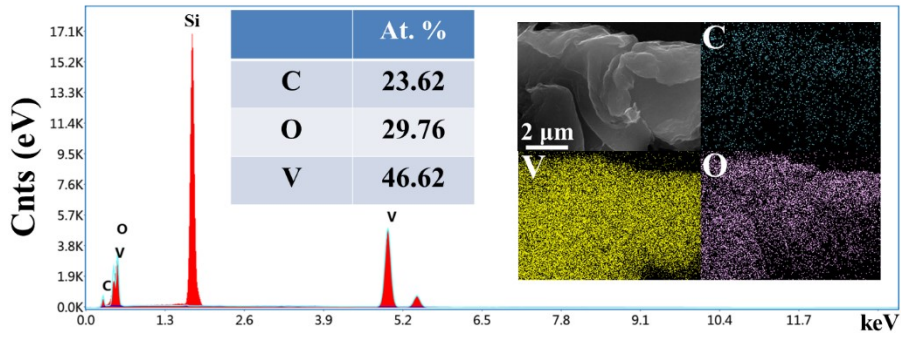

Fig. S4 EDS as well as elemental mappings of (2-M-AQ)-VO.

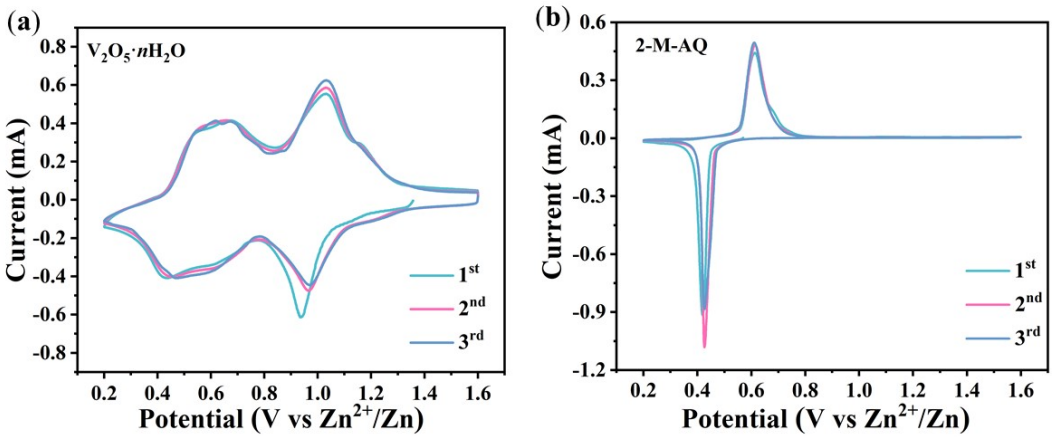

Fig. S5 The first three CVs of $V_2O_5 \cdot nH_2O$ and 2-M-AQ.

Table S2 The comparison of the electrochemical performances of (2-M-AQ)-VO and other vanadium-based materials.

Material	Specific capacity	Cycle number	Capacity retention	Reference
$Zn_{0.25}V_2O_5 \cdot nH_2O$	282 mAh g^{-1} at 0.3 A g^{-1}	1000 (2.4 A g^{-1})	80.0 %	4
δ-$Ni_{0.25}V_2O_5 \cdot nH_2O$	402 mAh g^{-1} at 0.2 A g^{-1}	1200 (5.0 A g^{-1})	98.0 %	5
MnVO	415 mAh g^{-1} at 0.05 A g^{-1}	2000 (4.0 A g^{-1})	92.0 %	6
$Li_xV_2O_5 \cdot n\ H_2O$	470 mAh g^{-1} at 0.05 A g^{-1}	1000 (10.0 A g^{-1})	93.0 %	7
$Mg_{0.34}V_2O_5 \cdot 0.84H_2O$	353 mAh g^{-1} at 0.05 A g^{-1}	2000 (5.0 A g^{-1})	97.0 %	8
AlVO	418 mAh g^{-1} at 0.2 A g^{-1}	1000 (5.0 A g^{-1})	90.5 %	9
PA-VOP	268.2 mAh g^{-1} at 0.1 A g^{-1}	2000 (5.0 A g^{-1})	92.3 %	10
PEDOT-NVO	356.8 mAh g^{-1} at 0.05 A g^{-1}	5000 (10.0 A g^{-1})	94.1 %	11
bilayer-VOP	313.6 mAh g^{-1} at 0.1 A g^{-1}	2000 (5.0 A g^{-1})	76.8 %	12
(2-M-AQ)-VO	**422 (286) mAh g^{-1} at 0.2 (1) A g^{-1}**	**1000 (1 A g^{-1}) 2000 (5 A g^{-1})**	**73.6 % 80.2 %**	**This work**
(2-M-AQ)-VO with Cu^{2+}	**433 (381) mAh g^{-1} at 0.2 (1) A g^{-1}**	**1000(1 A g^{-1}) 3200 (5 A g^{-1})**	**~ 100 % ~ 100 %**	**This work**

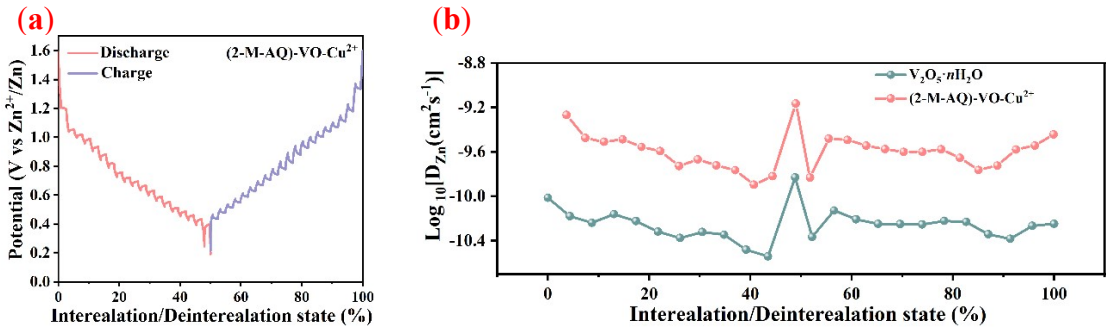

Fig. S6 (**a**) GITT profiles of (2-M-AQ)-VO-Cu^{2+}; (**b**) The calculated $D_{Zn^{2+}}$ in $V_2O_5 \cdot nH_2O$ and (2-M-AQ)-VO-Cu^{2+}.

Table S3 The parameters in the equivalent circuit for (2-M-AQ)-VO and $V_2O_5 \cdot nH_2O$.

Sample/Electrolyte		R_s (Ω cm^{-2})	R_{ct} (Ω cm^{-2})	CPE	W (Ω cm^{-2})
(2-M-AQ)-VO	$Zn^{2+} + Cu^{2+}$	1.40	2.60	4.0×10^{-2}	9.37
(2-M-AQ)-VO	Zn^{2+}	1.21	8.33	3.1×10^{-2}	10.57
$V_2O_5 \cdot nH_2O$	Zn^{2+}	1.44	12.66	5.8×10^{-3}	0.44

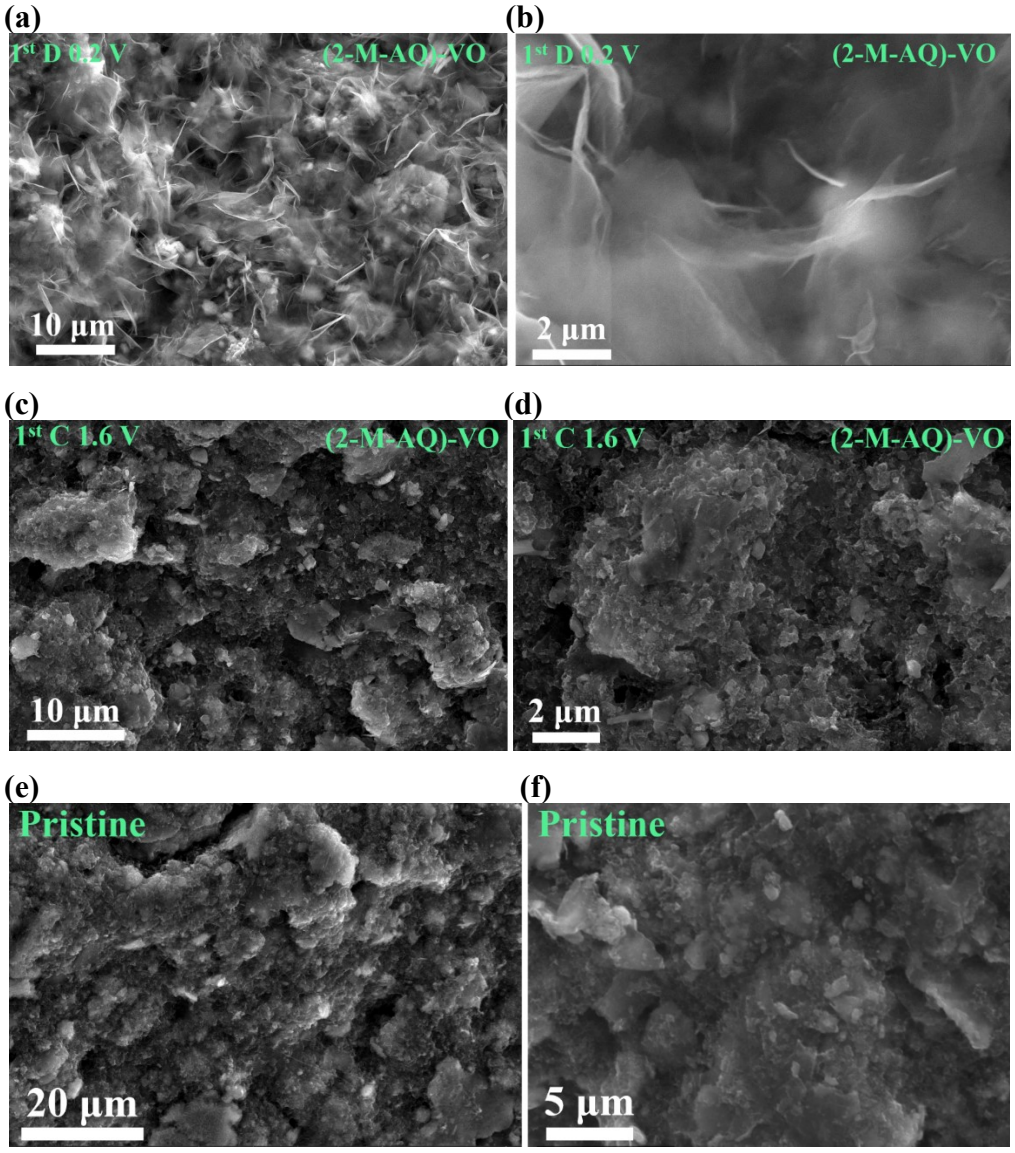

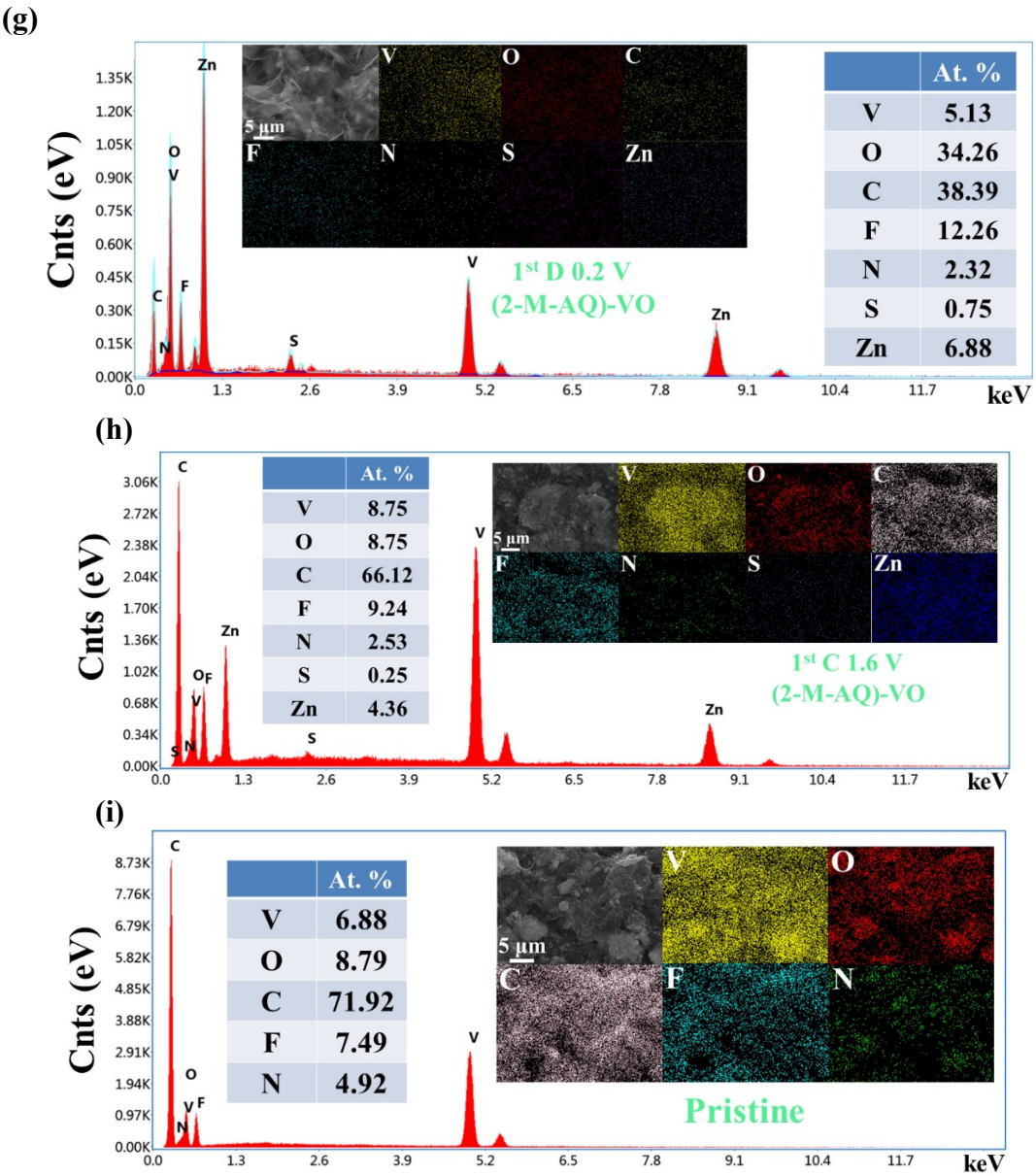

Fig. S7(a-f) *Ex situ* SEM images and (**g-i**) EDS as well as elemental mappings of the (2-M-AQ)-VO electrode in 3 M $Zn(CF_3SO_3)_2$ during the 1st discharge and charge process, including (**a, b, g**) discharge to 0.2 V, (**c, d, h**) charge to 1.6 V and (**e, f, i**) the pristine electrode.

Table S4 Element contents (at.%) of the (2-M-AQ)-VO electrode in the electrolytes with and without Cu^{2+} under different states.

At. %	Pristine	1st D 0.2	1st C 1.6	1st D 0.2 with Cu^{2+}	1st C 1.6 with Cu^{2+}
Cu	/	/	/	0.31	0.13
V	6.88	5.13	8.75	7.31	6.12
O	8.79	34.26	8.75	18.80	5.98
C	71.92	38.39	66.12	48.16	73.49
F	7.49	12.26	9.24	3.88	9.86
N	4.92	2.32	2.53	1.01	1.30
S	/	0.75	0.25	2.21	0.60
Zn	/	6.88	4.36	18.31	2.52

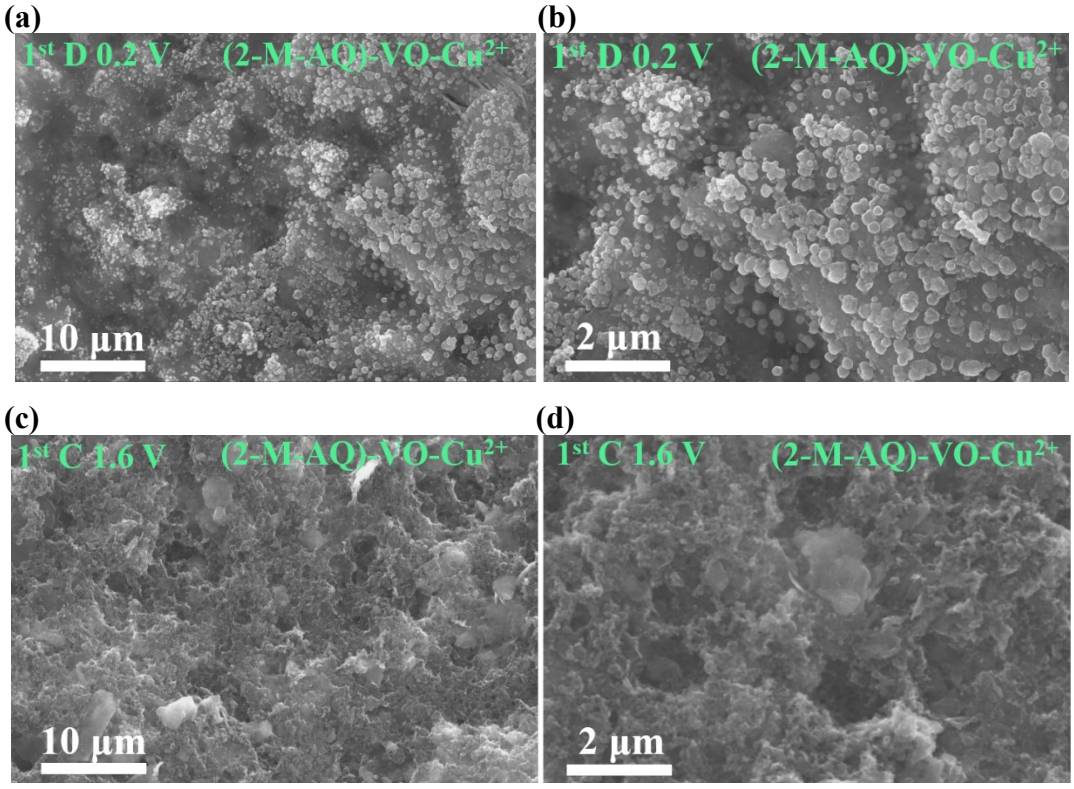

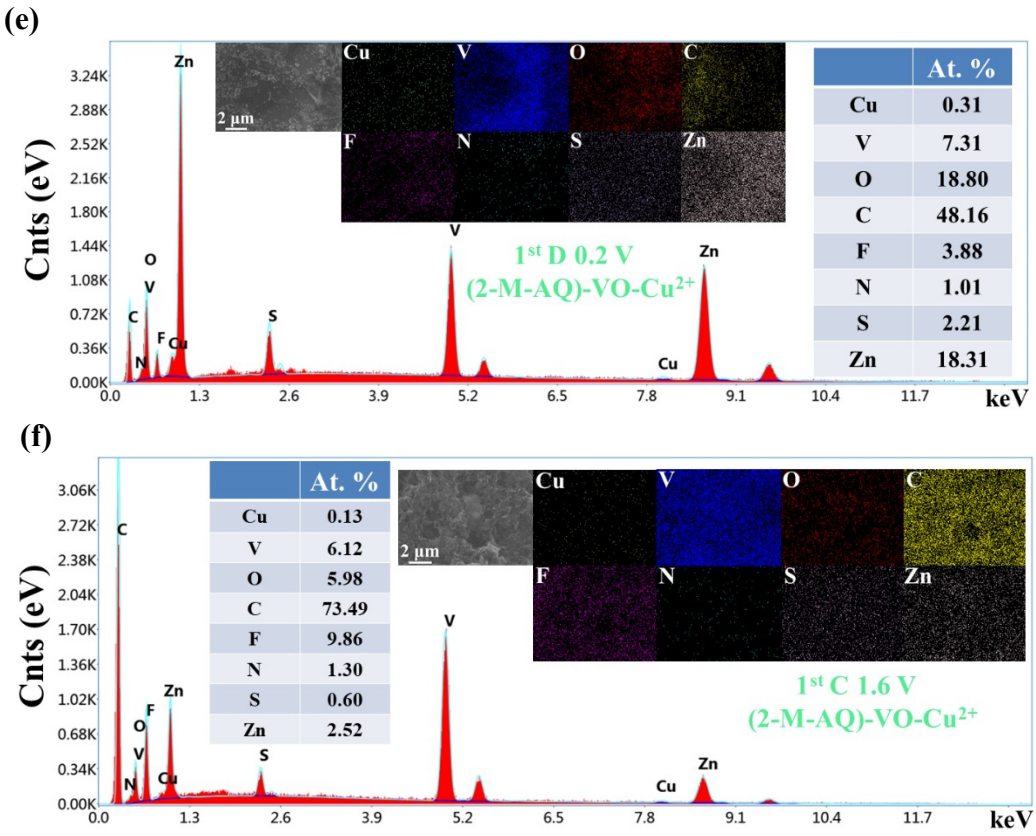

Fig. S8 (**a-d**) *Ex situ* SEM and (**e, f**) EDS as well as elemental mappings of the (2-M-AQ)-VO electrode in the electrolyte of 2.8 M $Zn(CF_3SO_3)_2$ and 0.2 M $CuSO_4$: (**a, b, e**) 1st discharge to 0.2 V and (**c, d, f**) charge to 1.6 V.

S2 *Ex situ* XPS spectra of the (2-M-AQ)-VO electrode in 3 M $Zn(CF_3SO_3)_2$

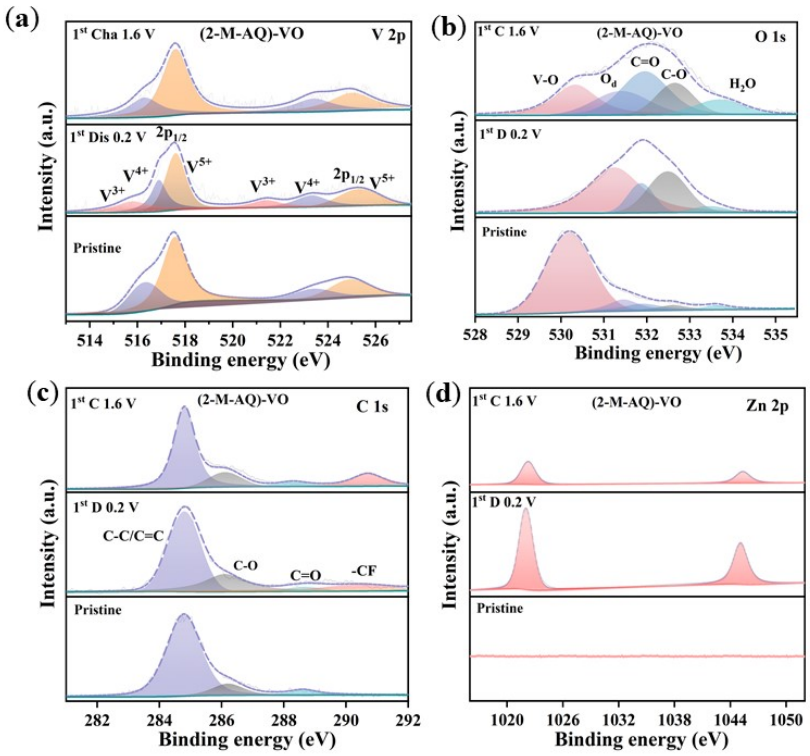

Fig. S9 *Ex situ* XPS of the (2-M-AQ)-VO electrode in 3 M $Zn(CF_3SO_3)_2$ at different states: (**a**) V 2p, (**b**) O 1s, (**c**) C 1s and (**d**) Zn 2p.

In addition, *ex situ* XPS of the (2-M-AQ)-VO electrode in 3 M $Zn(CF_3SO_3)_2$ have been measured. As shown in the **Fig. S9a**, the peaks located at 516.2 and 517.5 eV are assigned to V^{4+} $2p_{3/2}$ and V^{5+} $2p_{3/2}$ species, respectively.[13] And the peaks at 523.4 and 524.9 eV are indexed to V^{4+} $2p_{1/2}$ and V^{5+} $2p_{1/2}$, respectively.[13] When discharge to 0.2 V, V^{3+} signals appear at 515.9 ($2p_{3/2}$) and 521.4 eV ($2p_{1/2}$),[6, 8] and the V^{4+} signals are intensified along with the weakened of V^{5+} signals, suggesting that the partial reduction of V^{5+}/V^{4+} into V^{4+}/V^{3+}. The charge process is reverse, indicating the oxidization of $V^{4+}/V^{3+}\rightarrow V^{5+}/V^{4+}$ during the escape process of Zn^{2+} from (2-M-AQ)-VO. In the O 1s XPS fine spectra (**Fig. S9b**), the pristine AQ-VO electrode exhibits five peaks located at 530.2, 531.5, 531.9, 532.6 and 533.6 eV, which can be indexed to V-O, oxygen defect, C=O, C-O and H_2O, respectively.[14-16] When the first charged to 0.2 V, the

relative intensity of C=O group becomes weaker with the C-O signal intensified, which can be attributed to the reduction reaction of C=O + e^- → C-O in the discharge process. Then their relative intensities recover during the charge process, indicating the encouraging redox reversibility of the 2-M-AQ organic species. The C 1s fine spectra are presented in **Fig. S9c**, in which the variation tendencies of the C=O and C-O signals are consistent with those in the O 1s spectra. And the peak at 290.8 eV is ascribed to the -CF signal from the PVDF binder. **Fig. S9d** exhibits the Zn 2p spectra of the (2-M-AQ)-VO electrode at different states in the 1st cycle. No Zn signal is observed at the pristine state. And it is worth mentioning that the Zn 2p spectra of the (2-M-AQ)-VO electrode in the electrolyte without Cu^{2+} only exhibit the inserted Zn signals at 1022.2 ($2p_{3/2}$) and 1045.3 eV ($2p_{1/2}$) at the discharge/charge states (**Fig. S9d**), and the residual Zn signals at the fully charged state seems stronger than those in the presence of Cu^{2+}, suggesting that the reversibility of the Zn^{2+} (de)intercalation in 3 M $Zn(CF_3SO_3)_2$ is inferior to that in the presence of Cu^{2+}.

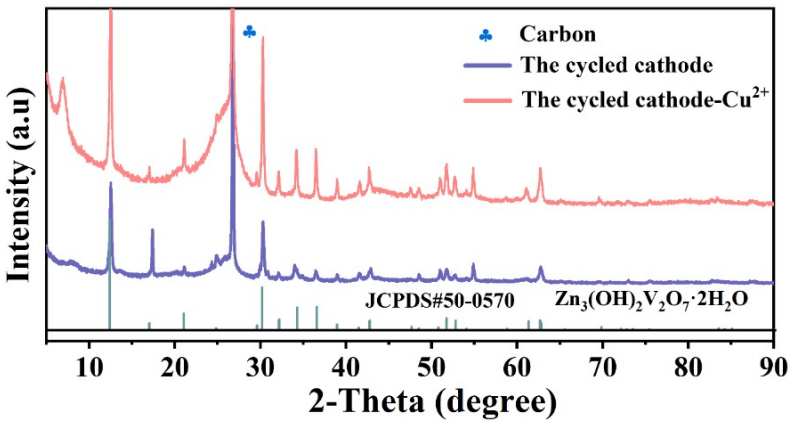

Fig. S10 XRD patterns of the (2-M-AQ)-VO electrodes in the electrolytes with and without Cu^{2+} after the cycling test at 1 A g^{-1}.

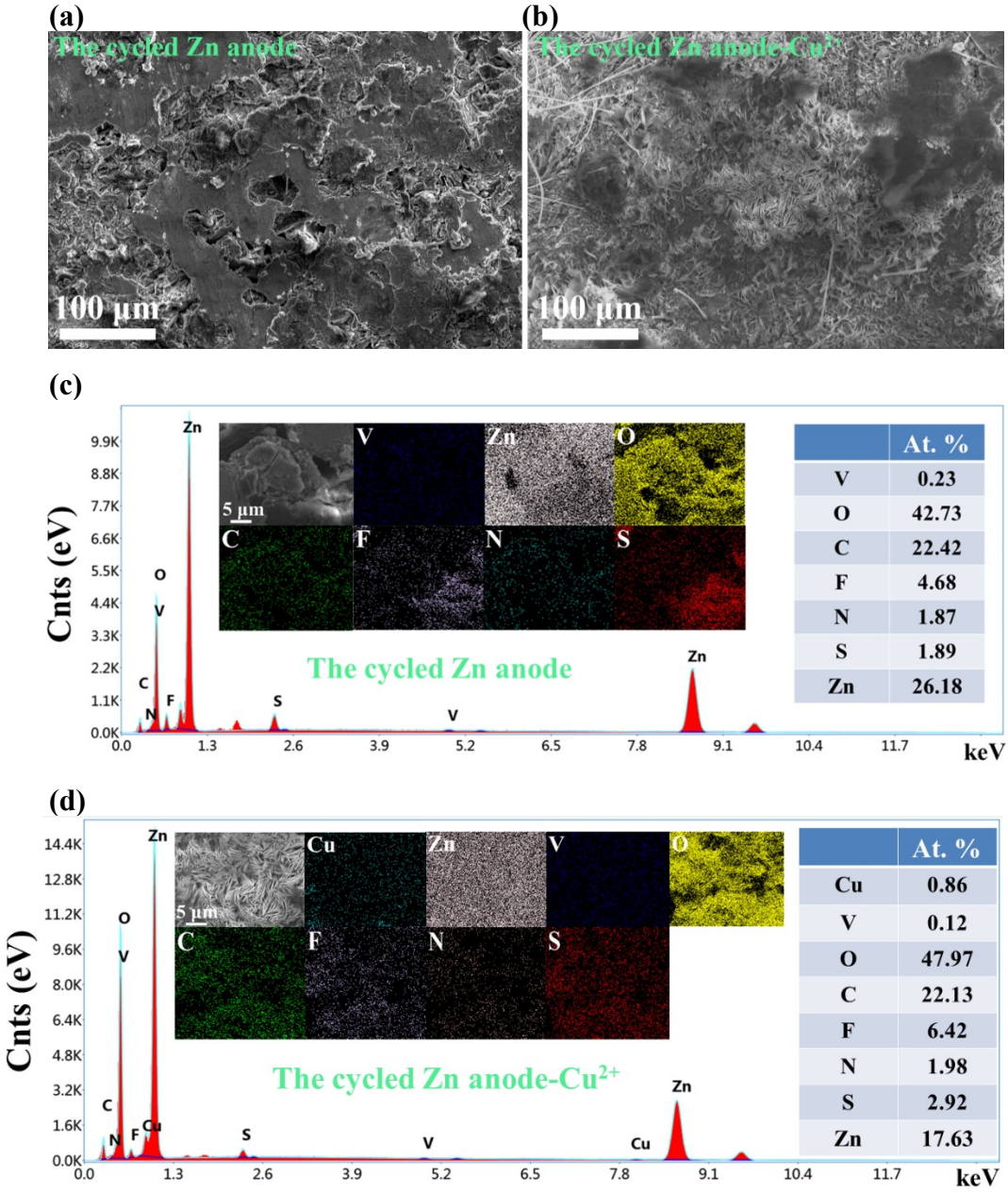

Fig. S11 (**a**, **b**) SEM images and (**c**, **d**) EDS as well as elemental of the cycled Zn anodes in the electrolytes (**b**, **d**) with and (**a**, **c**) without Cu^{2+}.

S3 The effect of the Cu^{2+} additive in the electrolyte on Zn foil in the Zn//Zn symmetrical cell

In aqueous ZIBs, inhomogeneous Zn deposition during continuous Zn stripping/plating processes would consume active Zn and electrolyte irreversibly to deteriorate the cycling durability.[17, 18] Due to the higher E^{θ} (Cu^{2+}/Cu^{+}) (0.159 V) than E^{θ} (Zn^{2+}/Zn) (-0.763 V), Cu^{2+} is preferential to gain electrons in comparison with Zn^{2+}. It is except that the Cu^{2+} additive in the electrolyte can modify the interface between Zn metal and electrolyte to prolong the cycling life of the Zn anode.

To verify the function of the Cu^{2+} cation in the electrolyte on Zn anode, the cycling performances of the Zn//Zn symmetrical cells were carried out comparatively in different electrolytes at a current density of 0.5 mA cm^{-2} and an areal capacity of 0.25 mAh cm^{-2}. As displayed in **Fig. S12a**, the positive effect of the Cu^{2+} additive on the Zn foil can be confirmed by the cycling test at a high current density of 5 mA cm^{-2} with an areal capacity of 1 mAh cm^{-2}. The Zn//Zn symmetrical cell displays a long lifespan of 450 h with a low plating/stripping overpotential (**Fig. S12a**, inset) in the electrolyte with Cu^{2+}, which is superior to the cell in the absence of Cu^{2+} (short-circuit after 75 h). The result indicates that the Cu^{2+} ion in the electrolyte plays a remarkably important role in the cycling stability of Zn anode.

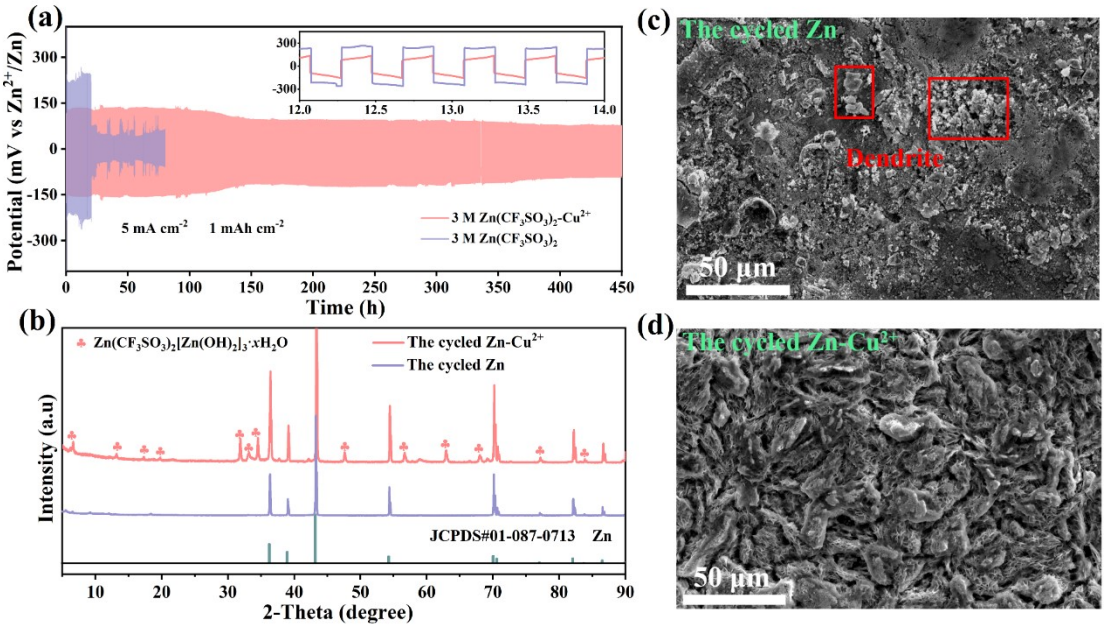

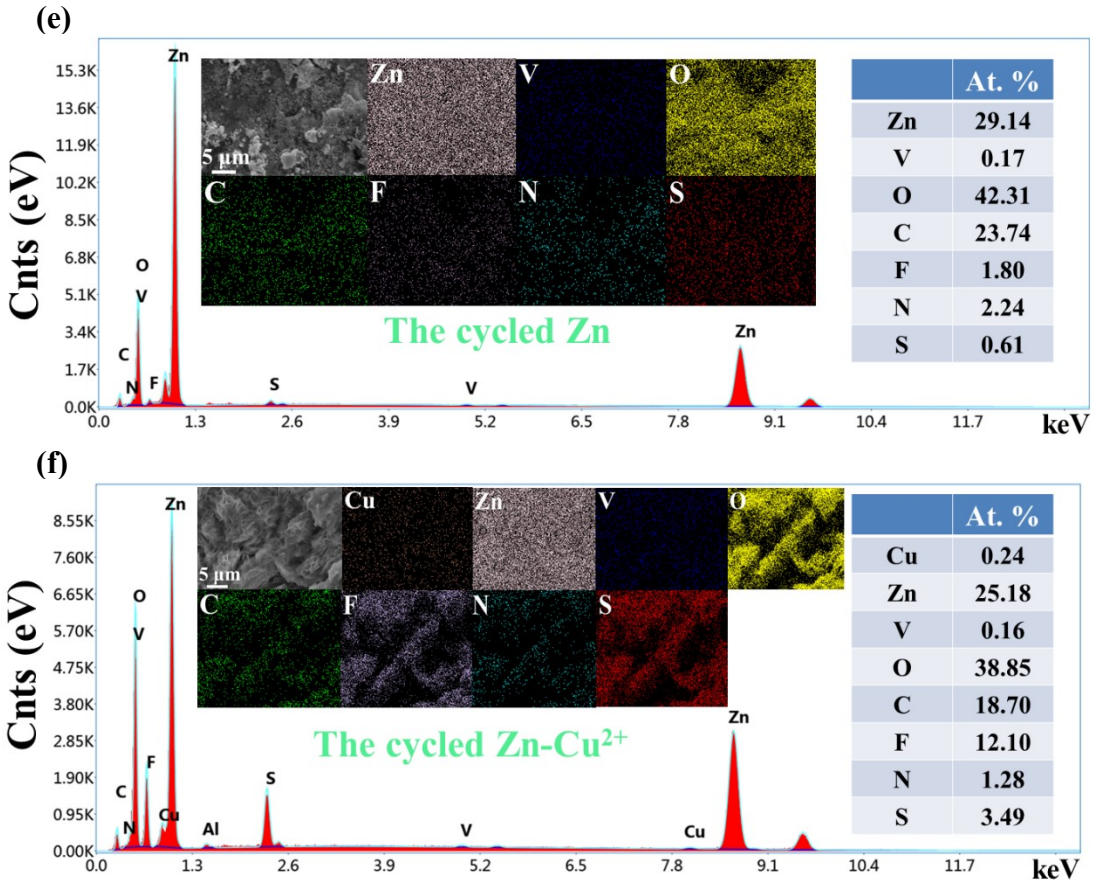

Fig. S12 (**a**) Cycling performance comparison of the Zn//Zn symmetrical cells at 5 mA cm^{-2} and 1 mAh cm^{-2} in different electrolytes; (**b**) XRD patterns and (**c**, **d**) SEM images of the cycled Zn foils in the electrolytes (**c**) without and (**d**) with Cu^{2+}. (**e**, **f**) EDS as well as elemental mappings of the cycled Zn anodes in the electrolytes (**c**, **e**) with and without (**d**, **f**) Cu^{2+} in Zn||Zn symmetrical cell.

In order to further reveal the reason for the improved long-term durability of Zn foil in the electrolyte with Cu^{2+}, the XRD patterns and SEM images of the cycled Zn foils in the electrolytes with and without Cu^{2+} have been measured. As displayed in **Fig. S12b**. except the diffraction peaks of zinc (PDF#01-87–0713), the others peaks can be indexed to the $Zn(CF_3SO_3)_2[Zn(OH)_2]_3 \cdot xH_2O$ phase. It is worth mentioning that the relative intensity of the $Zn(CF_3SO_3)_2[Zn(OH)_2]_3 \cdot xH_2O$ phase is much stronger when Cu^{2+} is present in the electrolyte.

SEM images of the cycled zinc foils are shown in **Fig. S12(c, d)**. In 3M $Zn(CF_3SO_3)_2$, the surface of the cycled Zn appears rock-like dendrites (**Fig. S12c**), indicating the heterogeneous Zn deposition/stripping in the aqueous electrolyte. In contrast, porous

and uniform microflake arrays are covered on the surface of the cycled Zn foil in the electrolyte with Cu^{2+} (**Fig. S12d**). Therefore, during the plating/stripping process, the porous microflake arrays on the surface not only can facilitate the penetration of the electrolyte to achieve uniform Zn^{2+} flux/ nucleation, but also can protect the Zn foil from corrosion. The corresponding EDS and elemental mappings of the cycled Zn foils are shown in **Fig. S12(e, f)**. It can be seen that in the electrolyte with Cu^{2+} additive, Cu (0.24 at. %) has incorporated into the cycled Zn foil with more F (12.10 at. %) and S contents (3.49 at. %) than those in the absence of Cu^{2+} (F: 1.80 at. %; S: 0.61 at. %), agreeing with the XRD patterns and SEM images.

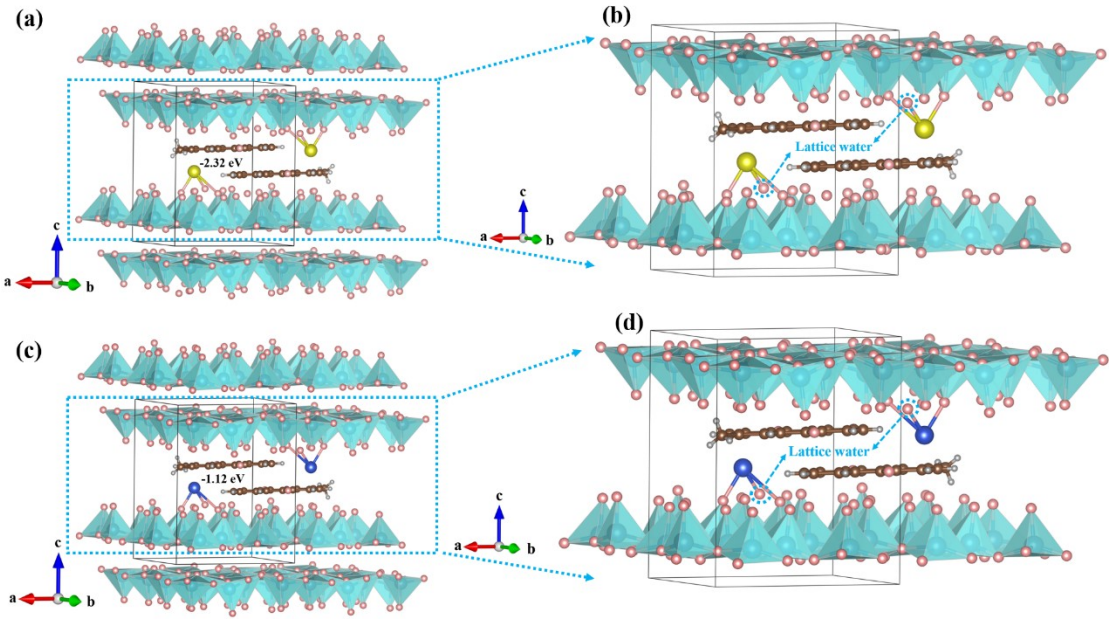

Fig. S13 The configuration of (**a**, **b**) the Zn^{2+} or (**c**, **d**) Cu^{2+} intercalated on the same site in the inner channel of (2-M-AQ)-VO; The magnified images of the blue squares in (**b**) **a** and (**d**) **c**.

Reference

1. G. Kresse and J. Furthmüller, *Comput. Mater. Sci.*, 1996, **6**, 15-50.
2. J. P. Perdew, K. Burke and M. Ernzerhof, *Phys. Rev. Lett.*, 1996, **77**, 3865-3868.
3. J. Behler, *J. Chem. Phys.*, 2011, **134**, 074106.
4. D. Kundu, B. D. Adams, V. Duffort, S. H. Vajargah and L. F. Nazar, *Nat. Energy*, 2016, **1**, 119.
5. J. Li, K. McColl, X. Lu, S. Sathasivam, H. Dong, L. Kang, Z. Li, S. Zhao, A. G. Kafizas, R. Wang, D. J. L. Brett, P. R. Shearing, F. Corà, G. He, C. J. Carmalt and I. P. Parkin, 2020, **10**, 2000058.

6. C. Liu, Z. Neale, J. Zheng, X. Jia, J. Huang, M. Yan, M. Tian, M. Wang, J. Yang and G. Cao, *Energy Environ. Sci.*, 2019, **12**, 2273-2285.
7. Y. Yang, Y. Tang, G. Fang, L. Shan, J. Guo, W. Zhang, C. Wang, L. Wang, J. Zhou and S. Liang, *Energy Environ. Sci.*, 2018, **11**, 3157-3162.
8. F. Ming, H. Liang, Y. Lei, S. Kandambeth, M. Eddaoudi and H. N. Alshareef, *ACS Energy Lett.*, 2018, **3**, 2602-2609.
9. Y. Liu, X. Xiao, X. Liu, L. L. Cui and Y. Gong, *J. Mater. Chem. A*, 2022, **10**, 912-927.
10. L. Hu, Z. Wu, C. Lu, F. Ye, Q. Liu and Z. Sun, *Energy Environ. Sci.*, 2021, **14**, 4095-4106.
11. D. Bin, W. Huo, Y. Yuan, J. Huang, Y. Liu, Y. Zhang, F. Dong, Y. Wang and Y. Xia, *Chem*, 2020, **6**, 968-984.
12. Z. Wu, C. Lu, F. Ye, L. Zhang, L. Jiang, Q. Liu, H. Dong, Z. Sun and L. Hu, *Adv. Funct. Mater.*, 2021, **31**, 2106816.
13. G. Silversmit, D. Depla, H. Poelman, G. B. Marin and R. De Gryse, *J. Electron. Spectrosc. Relat. Phenom.*, 2004, **135**, 167-175.
14. N. Zhang, M. Jia, Y. Dong, Y. Wang, J. Xu, Y. Liu, L. Jiao and F. Cheng, *Adv. Funct. Mater.*, 2019, **29**, 1807331.
15. S. Zhang, W. Zhao, H. Li and Q. Xu, *ChemSusChem*, 2020, **13**, 188-195.
16. H. Jiang, W. Gong, Y. Zhang, X. Liu, M. Waqar, J. Sun, Y. Liu, X. Dong, C. Meng, Z. Pan and J. Wang, *J. Energy Chem.*, 2022, **70**, 52-58.
17. J. Yin, X. Feng, Z. Gan, Y. Gao, Y. Cheng and X. Xu, *Energy Storage Mater.*, 2023, **54**, 623-640.
18. Q. Zhang, J. Luan, Y. Tang, X. Ji and H. Wang, *Angew. Chem. Int. Ed. Engl.*, 2020, **59**, 13180-13191.